

Excitonic states in spherical layered quantum dots

Mariano Garagiola^a, Omar Osenda^{a,*}

^a*Facultad de Matemática, Astronomía, Física y Computación, Universidad Nacional de Córdoba and Instituto de Física Enrique Gaviola, CONICET, Ciudad Universitaria, Córdoba, Argentina X5000HUA*

Abstract

The properties of excitons formed in spherical quantum dots are studied using the $\mathbf{k} \cdot \mathbf{p}$ method within the Hartree approximation. The spherical quantum dots considered have a central core and several concentric layers of different semiconductor materials that are modeled as a succession of potential wells and barriers. The $\mathbf{k} \cdot \mathbf{p}$ Hamiltonian and the Coulomb equations for the electron-hole pair are solved using a self-consistent iterative method. The calculation of the spectrum of the empty quantum dot and the electron-hole pair is performed by means of a very accurate numerical approximation. It is found that the exciton binding energy as a function of the core radius of the quantum dot shows a strong non-linear behaviour. In particular, for quantum dots with two potential wells, the binding energy presents a large steep change. This last behaviour is explained in terms of the polarization charges at the interfaces between different materials and the matching conditions for the eigenfunctions.

Keywords: excitons, spherical quantum dots, Hartree approximation

1. Introduction

The methods to produce multi-layered spherical quantum dots are well established for some years now [1, 2, 3, 4]. Their two-dimensional counterpart, also known as quantum rings, have a similar development. Both kind of settings, two and three-dimensional, have been used to experimentally test the foundations of the Quantum Mechanics theory and an increasing number of applications.

The confinement of electrons in semiconductor quantum dots is owed to different mechanisms. In assembled quantum dots, the confinement is produced by the mismatch between the energy bands of the different materials that compose the heterostructure. This mechanism is so used that the possible semiconductor heterojunctions are classified by its band alignment, types one, two and three, which are also known as straddling, staggered and broken gaps, respectively.

Quantum dot quantum well structures (QDQW), *i.e.* the spherical structures that have a spherical core made up of a wide gap semiconductor, a first layer surrounding the core (also known as the well) that is made up of a narrow gap material, and a second layer made up with a wide gap material, have been extensively studied, in particular the CdS/HgS/CdS QDQW [5, 6, 7, 8, 9].

The number of layers to consider in a given structure is chosen to meet some design requirement. In the case QDQW structures, the desired effect was the increasing of the cross section of the confined electrons, with respect to a simple QD with a similar total radius [10].

The energy gaps characteristic of the semiconductor materials that made up the most common multi-layered quantum dots are bounded between 1.5 and 3 eV or even higher values so, at low or even ambient temperatures, the conduction band is empty and the promotion of electrons from the valence band to the conduction one is achieved applying electromagnetic fields with optical or near optical frequencies. As a matter of fact, the study of this type of structures and materials is fueled by its possible application to

*Corresponding author

Email addresses: mgaragiola@famaf.unc.edu.ar (Mariano Garagiola), osenda@famaf.unc.edu.ar (Omar Osenda)

construct solar cells or light emitting diodes [11, 12]. Once an electron is promoted from the valence band to the conduction one the hole left by the electron interacts with it, forming an electron-hole pair. more commonly known as an exciton [13, 14]. Of course, this is a simple, and partial, description of the many-body response of all the electrons involved [15, 16, 17]. Anyway, the absorption lines observed in many experiments confirm that the description in terms of two interacting particles of opposite charge has a very broad range of validity and the theoretical calculations made in models formulated within this description predict the experimental findings more or less accurately .

The simplest model that captures the two-particle description of an exciton is formulated using the Effective Mass Approximation (EMA) approach [6, 7, 9, 16, 18, 19] . In this approximation the electron and hole physics is described using Schrödinger-like equations that depend on effective parameters for the masses of both electron and hole. Besides, the interaction between the pair is given by a Coulomb potential that includes a macroscopic dielectric constant, and the confinement potential is provided by piecewise potentials that model the band structure profile of the nanostructure. The model with all the ingredients mentioned before is also known as the one-band EMA, since the electron and hole are indeed confined to the conduction and valence bands, respectively. Despite all the assumptions involved the energy spectrum that results from the one-band EMA model, when it is applied to a single electron, is surprisingly good, so this model finds its natural application in the modeling of electrons confined in two- and three-dimensional electrostatically induced quantum dots, where the charging of the dot is achieved, for instance, lowering the electrostatic barriers that define the dot or connecting it to “electron reservoirs” through metallic leads, so neither an electron is promoted from the valence to the conduction band nor a exciton is formed.

A more sophisticated approach to deal with the band structure employs the $\mathbf{k} \cdot \mathbf{p}$ model [20, 21] which, as the EMA, depends on a number of effective parameters, but incorporates in a more natural fashion the crystal structure of the materials, the interaction between the energy bands, mechanical strain [22, 23, 24], spin-orbit interaction and so on. Besides, the results calculated using the $\mathbf{k} \cdot \mathbf{p}$ are more accurate than those obtained using the EMA approximation and closer to the experimental ones [25, 26]. It is important to note that the spectrum obtained using the method corresponds to the “empty” dot so, if the excitonic energies are to be calculated, the interaction between a particle occupying a level below the gap and other occupying a level above the gap must be introduced, again, assuming that it takes the form of a known potential [27, 28, 29]. The optical selection rules prevent that all the excitons that can be formed could be excited in a direct fashion. The lowest lying exciton is called “dark exciton” (DE) precisely for this reason, while the excitons that can be optically excited are conversely termed “bright excitons” (BE) [30]. Depending on the nanostructure under study the DE recombination strongly modifies its photoluminescence properties at low temperatures. At any rate, the ground exciton state is studied on its own to characterize the physical traits of nanostructures or bulk materials in many different situations. The dark and bright excitons spectrum can be calculated effectively using the $\mathbf{k} \cdot \mathbf{p}$ method by introducing an effective electron-hole interaction and constructing electron and hole wave functions with definite angular momentum quantum numbers [30].

It is worth to mention that since excitons in semiconductor devices are less susceptible to perturbations produced by phonons than single electrons, once an exciton is formed its mean lifetime might be long enough to implement Quantum Information tasks [31, 32]. This fact has led to numerous attempts to identify systems where the coherent control, readout and initial preparations of excitonic states can be performed accurately and in a reliable way.

There is not a reason to limit the number of layers to a core, a well and a barrier and it has been shown that spherical layered dots with two wells have some remarkable properties [9, 33, 34, 35, 36, 37, 38] , in particular the EMA model for a single electron confined in the dot predicts that the wave function of few excited states can be located in the innermost well while the the wave function of all the other eigenstates is located in the outermost well [34]. By located in a well it is understood that the probability that the electron is outside a given well is negligible. In Reference [34] it was shown that the number of eigenstates located in the innermost well can be tuned precisely changing the radius of the core, while in Reference [33] the localization phenomenon was studied only for the ground state.

In view of the results obtained using the EMA approach with respect to the localization properties of the electron wave function in spherical layered QD, it is reasonable to wonder about the behaviour of an exciton in this kind of structure when it is studied using the $\mathbf{k} \cdot \mathbf{p}$ model. Moreover, since the electron

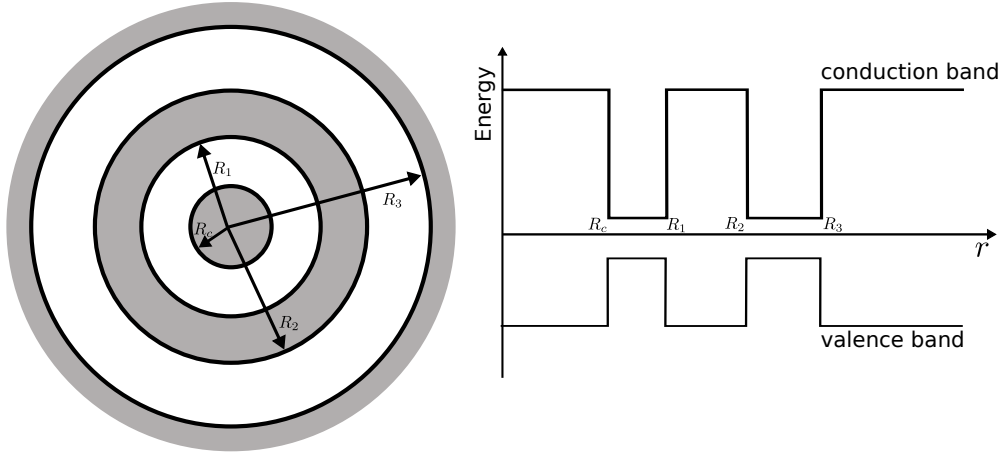


Figure 1: The cartoon on the left depicts the cross-section of a ZnS/CdSe/ZnS/CdSe/ZnS structure. A grey zone correspond to a layer (or core) of ZnS, while a white zone correspond to a layer of CdSe. The core radius, R_c and the outermost radius of each layer, R_1 , R_2 and R_3 are also shown. The top of the valence band and the bottom of the conduction one are sketched as functions of the radial coordinate on the right side of the Figure.

and the hole have different effective masses it is to be expected that their localization properties differ from what it is observed in the EMA approach for a single electron. The goal of the present study is to characterize the behaviour of an exciton bounded in a spherical layered quantum dot with two wells, using the $\mathbf{k} \cdot \mathbf{p}$ model to obtain the energy bands of the nanostructure. The manuscript is organized as follows, the modelling of spherical layered QDs and the $\mathbf{k} \cdot \mathbf{p}$ model are depicted in Section 2, while the properties of the spectrum, eigenstates and excitons in structures with one or two wells are shown in Section 3. The spectrum and eigenfunctions are obtained using a high-precision Rayleigh-Ritz variational method. In Section 4 we summarize and discuss our results. Most technical details about the variational method, the variational basis set functions are referred to Appendices.

2. Brief description of the layered QD structures and the $\mathbf{k} \cdot \mathbf{p}$ model

Besides the core, wells and barriers structure, some models of multilayered quantum dots include some cladding, usually a dielectric material with a band gap larger than the gap of the materials that form the quantum dot. This amounts for an homogeneous boundary condition for the wave functions. The model considered in this Section do not have a cladding, instead of that it is supposed that the outermost barrier extends indefinitely. In Figure 1 a cartoon is used to depict the layered structure associated to the quantum dot. The target-like graph depicts, using gray and light rings the barriers and wells present in the quantum dot, respectively, while the central disk corresponds to the core. The band structure profile is shown schematically as a function of the distance to the center of the QD. Along the work we use the known parameters of the semiconductors *ZnS* and *CdSe*, this allows us to compare with results previously obtained using the EMA approach in Reference [34] for a ZnS/CdSe/ZnS/ CdSe/ZnS QD. Along this work the core radius is denoted by R_c , while the other radii will be denoted as R_1 , R_2 , R_3 and so on, see Figure 1.

The $\mathbf{k} \cdot \mathbf{p}$ method has a huge number of variants that allow to include in the model a great deal of information about the semiconductor materials used to construct a given QD. Because the materials included in the layered QD that we intend to study the 8-band model for a zincblende crystal structure is the natural choice, its Hamiltonian given by [21, 39, 40]

$$H = \begin{pmatrix} A & 0 & V^* & 0 & \sqrt{3}V & -\sqrt{2}U & -U & \sqrt{2}V^* \\ 0 & A & -\sqrt{2}U & -\sqrt{3}V^* & 0 & -V & \sqrt{2}V & U \\ V & -\sqrt{2}U & -P+Q & -S^* & R & 0 & \sqrt{\frac{3}{2}}S & -\sqrt{2}Q \\ 0 & -\sqrt{3}V & -S & -P-Q & 0 & R & -\sqrt{2}R & \frac{1}{\sqrt{2}}S \\ \sqrt{3}V^* & 0 & R^* & 0 & -P-Q & S^* & \frac{1}{\sqrt{2}}S^* & \sqrt{2}R^* \\ -\sqrt{2}U & -V^* & 0 & R^* & S & -P+Q & \sqrt{2}Q & \sqrt{\frac{3}{2}}S^* \\ -U & \sqrt{2}V^* & \sqrt{\frac{3}{2}}S^* & -\sqrt{2}R^* & \frac{1}{\sqrt{2}}S & \sqrt{2}Q & -P-\Delta & 0 \\ \sqrt{2}V & U & -\sqrt{2}Q & \frac{1}{\sqrt{2}}S^* & \sqrt{2}R & \sqrt{\frac{3}{2}}S & 0 & -P-\Delta \end{pmatrix}, \quad (1)$$

where the entries in Equation (1) are given by

$$A = E_c + \frac{\hbar^2 k^2}{2m_0}, \quad (2)$$

$$P = -E_v + \gamma_1 \frac{\hbar^2 k^2}{2m_0}, \quad (3)$$

$$Q = \gamma_2 \frac{\hbar^2}{2m_0} (k_x^2 + k_y^2 - 2k_z^2), \quad (4)$$

$$R = -\sqrt{3} \frac{\hbar^2}{2m_0} [\gamma_2 (k_x^2 - k_y^2) - 2i\gamma_3 k_x k_y], \quad (5)$$

$$S = \sqrt{3}\gamma_3 \frac{\hbar^2}{m_0} k_z (k_x - ik_y), \quad (6)$$

$$U = \frac{i}{\sqrt{3}} P_0 k_z, \quad (7)$$

$$V = \frac{i}{\sqrt{6}} P_0 (k_x - ik_y), \quad (8)$$

where E_c is the energy at the bottom of the conduction band, E_v the energy at the top of the valence band, so $E_g = E_c - E_v$ is the band gap, γ_1 , γ_2 y γ_3 are the Luttinger parameters, Δ is the intensity of the spin-orbit interaction, P_0 the interaction strength between both bands, and this quantity is related to the Kane's energy, E_p , by

$$E_p = \frac{2m_0 P_0^2}{\hbar^2}. \quad (9)$$

For fixed values of k_x , k_y and k_z the Hamiltonian has eight eigenvalues, one for each sub-band. The largest pair belong to the conduction band, while the other six belong to the valence band and are the origin of the well known heavy-hole, light-hole, and split-off sub-bands. For a material without spin-orbit interaction each sub-band is doubly-degenerate, but in materials with a large spin-orbit interaction the degeneracy is broken.

As has been said above, the eight band Hamiltonian depends on the crystal structure, which is introduced via the Bloch functions, in our case the eight Bloch functions are given by

$$u_{1/2}^c = S \uparrow, \quad (10)$$

$$u_{-1/2}^c = S \downarrow, \quad (11)$$

$$u_{3/2,3/2}^v = \frac{1}{\sqrt{2}}(X + iY) \uparrow, \quad (12)$$

$$u_{3/2,1/2}^v = \frac{i}{\sqrt{6}}[(X + iY) \downarrow - 2Z \uparrow], \quad (13)$$

$$u_{3/2,-1/2}^v = \frac{1}{\sqrt{6}}[(X - iY) \uparrow + 2Z \downarrow], \quad (14)$$

$$u_{3/2,-3/2}^v = \frac{i}{\sqrt{2}}(X - iY) \downarrow, \quad (15)$$

$$u_{1/2,1/2}^v = \frac{1}{\sqrt{3}}[(X + iY) \downarrow + Z \uparrow], \quad (16)$$

$$u_{1/2,-1/2}^v = \frac{i}{\sqrt{3}}[-(X - iY) \uparrow + Z \downarrow], \quad (17)$$

where the supraindexes c and v correspond to the conduction and valence band, respectively, and S denotes a function that has spherical symmetry, while X , Y and Z are functions that combined have the same symmetry that Y_{1m} , *i.e.* the spherical harmonics with quantum number $\ell = 1$, for instance $X + iY$ has the same symmetry as Y_{11} . The parameters that enter in Equation 1 are matrix elements that must be calculated using the functions in Equations 10–17 but, usually, are phenomenologically determined. Nevertheless, since the Bloch basis gives the precise ordering of the matrix elements in Equation 1 we present them explicitly.

To obtain the band structure of a given nano-structure k_x, k_y and k_z cannot be considered parameters, as is the case for the bulk. Instead, the transformation $k_j = -i\frac{\partial}{\partial x_j}$ with $j = x, y, z$ leads the matrix Hamiltonian in Eq. 1 to a set of eight coupled Schrödinger-like equations, whose eigenvalues give the band structure of the nanodevice.

So, calling H the 8×8 differential operator that is obtained from Eq. 1, we look for the eigenvalues and eigenfunctions given by

$$H \Psi(\mathbf{r}) = E \Psi(\mathbf{r}), \quad (18)$$

where $\Psi(\mathbf{r})$ is a column vector

$$\Psi(\mathbf{r}) = \begin{pmatrix} \psi_1(\mathbf{r}) \\ \psi_2(\mathbf{r}) \\ \psi_3(\mathbf{r}) \\ \psi_4(\mathbf{r}) \\ \psi_5(\mathbf{r}) \\ \psi_6(\mathbf{r}) \\ \psi_7(\mathbf{r}) \\ \psi_8(\mathbf{r}) \end{pmatrix}. \quad (19)$$

The parameters of the materials that form the QD's to be studied are given in Table 1 and Table 2-

The band structure of a layered QD must be obtained solving the eigenvalue problem in Equation 18, considering the parameters as spatial functions. For instance, if r , the radial coordinate, is such that $r < R_c$ then the parameters are taken as the ones of the ZnS , while if $R_c < r < R_b$, then the parameters correspond to those of the $CdSe$ semiconductor, and so on. This is the case for the effective masses, the energy gap, the Kane's energy, the Luttinger parameters, etc. The discontinuity introduced in the material parameters, particularly for the masses, suggests that some care must be exercised to ensure that the problem is Hermitian [5, 34] and that this care must be extended to the matching conditions for the functions ψ_i at the interfaces between two different semiconductors.

In the Appendices Appendix A, Appendix B and Appendix C we briefly present the necessary details to implement a variational calculation of the eigenvalues and eigenfunctions, Equation 18, using a B-splines basis set [42, 41]. Some extra steps can be found in [34, 43] and References therein.

There are several forms to deal with the interaction between the electron-hole pair, but the two that attract more attention deal with it assuming a Coulomb-like potential [6, 9, 18, 27, 44] or consider that the interaction is the solution of the Poisson equation within some approximation. For instance, within the Hartree approximation [19, 22] it is assumed that the wave function of the pair is given by $\Psi(\mathbf{r}_e, \mathbf{r}_h) = \psi_e(\mathbf{r}_e)\psi_h(\mathbf{r}_h)$ where $\psi_e(\mathbf{r}_e)$ y $\psi_h(\mathbf{r}_h)$ are the wave functions of the electron and hole, respectively. Both one-particle wave functions are self-consistently calculated solving the eigenvalue problems

$$[H + V_e] \psi_h = \tilde{E}_h \psi_h, \quad (20)$$

$$[H + V_h] \psi_e = \tilde{E}_e \psi_e, \quad (21)$$

where \tilde{E}_e and \tilde{E}_h are eigenvalues that belong to the conduction and valence bands, respectively. The electrostatic potentials V_e and V_h are the solutions of a pair of Poisson equations

$$-e|\psi_e|^2 = \epsilon_0 \nabla (\epsilon_s(\mathbf{r}) \nabla V_e), \quad (22)$$

$$e|\psi_h|^2 = \epsilon_0 \nabla (\epsilon_s(\mathbf{r}) \nabla V_h). \quad (23)$$

The potentials V_e and V_h are continuous functions, but at the interfaces between two material the normal derivative is discontinuous because of the different dielectric constants of the materials at both sides of a interface. The problem of the polarization charges induced at the interface surfaces has been treated extensively [29, 17, 8, 45, 23]. The calculation method that is used to obtain the results reported in the next Section, a variational approach using *B*-splines functions as basis set, allows us to introduce the matching conditions for the functions ψ_i and the potentials explicitly. So, in our results the effects of the polarizations charges is included in the solutions of the Poisson Equations 22 and 23.

In Equations 20 and 21 H is the eight band Hamiltonian, and $\epsilon_s(\mathbf{r})$ is the dielectric constant as a function of the position along the radial coordinate of the QD.

The system of equations formed by Equations 20, 21, 22 and 23 is solved iteratively, using as a starting point the solutions found for the “empty” QD, Equation 18, to calculate the potentials V_e and V_h through Equations 22, 23 and then these potentials are introduced in Equations 20,21. New wave functions are calculated, which are then used to obtain new potentials and so on, until the energies obtained are stabilized. Again, the details of the procedure are deferred to the Appendices. In the following we denote as ψ_e^0 and ψ_h^0 the eigenfunctions of the empty QD that correspond to eigenvalues above and below the energy gap and that will be used as the starting point of the iterative solution of Equations 22,23. *A priori* any pair of electron E_e, ψ_e^0 , and hole E_h, ψ_h^0 energies and eigenfunctions could be used to calculate exciton binding energies but, most commonly, the calculation is restricted to the lowest and highest eigenvalues on the conduction and valence bands, respectively, and their respective eigenfunctions or, in other words, we focus in the dark exciton energy.

Finally, once stabilized values of the energies \tilde{E}_h and \tilde{E}_e are obtained, the binding energy can be calculated as

$$E_b = (E_e - E_h) - (\tilde{E}_e - \tilde{E}_h) = (E_e - \tilde{E}_e) + (\tilde{E}_h - E_h), \quad (24)$$

where E_e and E_h are energy values taken from the spectrum in Equation 18 that where used, together with their respective eigenfunctions, as the first step in the iteration procedure described above. Most commonly, E_e is taken as the lowest energy eigenvalue in the conduction band, while E_h is the highest energy eigenvalue in the valence band. Proceeding along these lines, $(E_e - E_h) - E_b$ is the lowest energy that a photon should have to promote an electron from the valence to the conduction band.

3. Results

3.1. A QDQW structure made of CdS/HgS/CdS

To check the correct implementation of the different algorithms a QDQW structure with a CdS core and barrier, and a HgS well was studied thoroughly. The election of the materials allows us to compare with results previously obtained using the EMA approach. All the parameters used to determine the $\mathbf{k} \cdot \mathbf{p}$ Hamiltonian can be found in Table 1.

Table 1: Parámetros de los materiales CdS y HgS utilizados en el punto cúbico.

	E_g	E_p	Δ	ϵ	γ_1	γ_2	γ_3
CdS	2.42 eV	19.6 eV	0.08 eV	5.5	0.814	0.307	0.307
HgS	0.42 eV	21.0 eV	0.08 eV	11.36	12.2	4.2	4.2

$$\text{CBO} = 1.35 \text{ eV}$$

$$\text{VBO} = 0.65 \text{ eV}$$

In the Table above CBO stands for the *conduction band offset*, i.e. the energy difference between the bottom of the conduction bands of both materials, while VBO stands for the *valence band offset*, which is the difference between the top of the valence bands for both materials.

The results for the energy spectrum, the Hartree energy levels and the binding energy are summarized in Figures 2, 3 and 4 respectively. The structure studied has a core with radius R_c and the well is characterized by two radii, the innermost one R_c and the outermost one, $R_1 = 15 \text{ nm}$.

Figure 2a) shows the lowest lying variational eigenvalues calculated using the $\mathbf{k} \cdot \mathbf{p}$ and EMA models *vs* the core radius. The number of bound states decreases when the core radius increases. The sets of eigenvalues calculated using the EMA and the $\mathbf{k} \cdot \mathbf{p}$ method are remarkably close which, to some extent, is to be expected since the interaction between bands and other effects that the $\mathbf{k} \cdot \mathbf{p}$ method takes into account (and the EMA method not) are relatively weak for the materials and QD dimensions considered. The valence band eigenvalues, shown in Figure 2b), also for both the $\mathbf{k} \cdot \mathbf{p}$ and EMA models, behave similarly to those in the conduction band. An appreciable difference can be observed for small core radius where the spectrum obtained with the $\mathbf{k} \cdot \mathbf{p}$ model shows some avoided crossings, signaling that for those R_c values the interaction between the different bands is large enough. On the other hand, the eigenvalues obtained from the EMA are smooth and can not show any avoided crossing see, for instance Reference [34] and References therein.

An important difference between the EMA approach and the $\mathbf{k} \cdot \mathbf{p}$ method arises because the Hamiltonian of the second, Equations 1, has terms that do not commute with the orbital angular momentum operator, \mathbf{L}^2 , see Equations 5, 6, 7 and 8. This has at least two consequences, the first has to do with the labeling of the eigenfunctions and eigenvalues in both methods. In the EMA, the inclusion of orbital angular momentum has the only effect that the radial potential changes and that the quantum numbers of the eigenfunctions and eigenvalues are the radial and the angular momentum ones, this is not true for the eigenfunctions and eigenvalues obtained using the $\mathbf{k} \cdot \mathbf{p}$ Hamiltonian. Second, the basis set necessary to implement a variational approximation for the EMA approach has functions that only depend on the radial coordinate, while the basis set of to implement the variational calculation in the $\mathbf{k} \cdot \mathbf{p}$ approach requires functions that depend on the radial and angular coordinates, see Appendix Appendix C. The second argument explains why it is easier to obtain a larger number of bounded eigenfunctions with the EMA approach than with the $\mathbf{k} \cdot \mathbf{p}$ approach. The energy of the eigenvalues in the EMA approach strongly depends on the radial quantum number but more weakly with the angular momentum quantum number (see Reference [34]).

Figure 3 shows the Hartree eigenvalues \tilde{E}_h and \tilde{E}_e , Equations 20 and 21, corresponding to the highest and lowest eigenvalues of the valence and conduction band, respectively, while Figure 4 shows the binding energy *vs* the core radius, R_c .

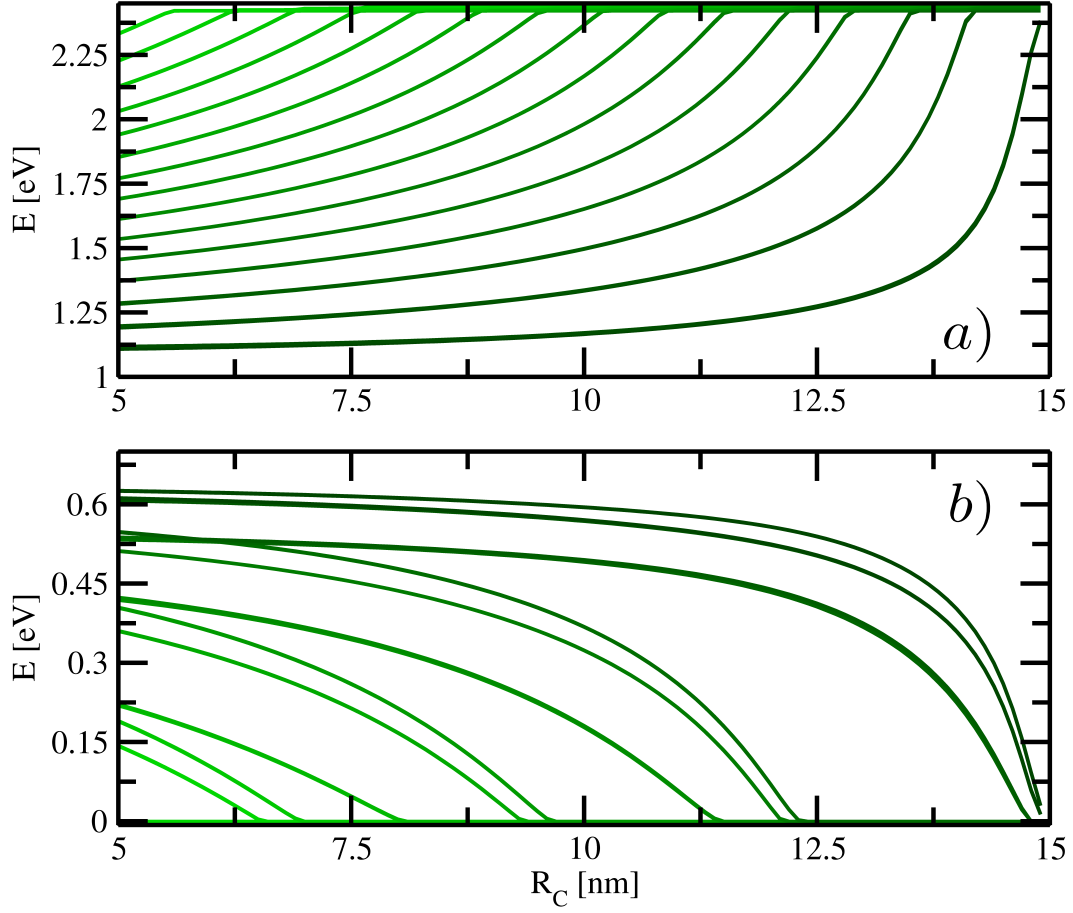


Figure 2: The variational eigenvalues calculated for the spherical QDQW structure CdS/HgS/CdS, for both the EMA (green curves) and $\mathbf{k} \cdot \mathbf{p}$ (black curves) approaches. a) Energy levels on the conduction band. b) Energy levels on the valence band.

The iterative procedure to solve simultaneously the Poisson equations and the $\mathbf{k} \cdot \mathbf{p}$ Hamiltonian converges rapidly, for all the values shown in Figure 4a) and b) the procedure converged after less than ten iterations. As it is to be expected, the interaction between the hole and the electron leads to a positive correction for the eigenvalue located in the valence band, and a negative one for the conduction band eigenvalue.

The behaviour of the binding energy, shown in Figure 4 merits a detailed analysis. At least since the work of Bryant [7], it is well known that the energy of an exciton decreases with the width of the potential well. Using perturbation theory, it is rather direct to show that the exciton binding energy decays as $1/L^\alpha$, where L is the width of the well in the QDQW structure, and α is some exponent. If the interaction between the hole and electron pair is given by a simple Coulomb term, α is, with a good accuracy, a natural number. Otherwise, if the interaction between the electron and the hole is not included only in terms of a Coulomb-like term, and the effects of polarization charges are taken into account the simple decaying behaviour can not be observed. In a QDQW structure there are several parameters that can be changed, we choose to keep the external well radius fixed and change the core radius, R_c , so when the core radius decreases the actual width of the well is being increased. This explains why the binding energy grows when R_c goes from 12.5 nm to 15 nanometers. For From $R_c \simeq 12.5$ to $R_c \rightarrow 0$ the binding energy grows when the width of the potential well increases. This behaviour is owed to the non-linear effects of the polarization charges and the change in the boundary condition at the center of the QD core.

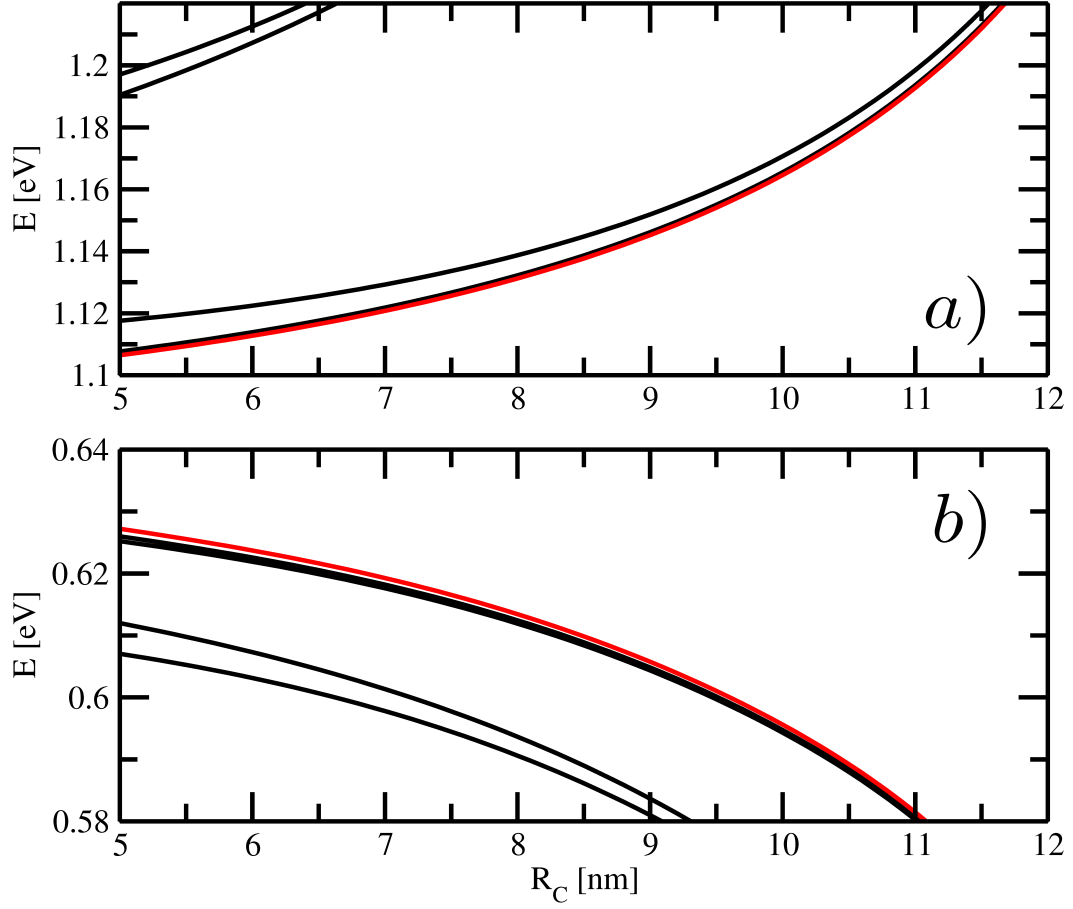


Figure 3: *a)* Eigenvalues on the conduction band. *b)* eigenvalues on the valence band. Both panels show a few eigenvalues that lie near the energy gap corresponding to the empty QD (black curves). The eigenvalues obtained implementing the Hartree approximation for the lowest eigenvalue of the conduction band and the higher one of the valence band (and corresponding eigenstates) are shown as red curves in both panels. It is clear that the energy gap predicted by the Hartree approximation is smaller than the gap of the empty QD.

3.2. A QD structure made of ZnS/CdSe/ZnS/CdSe/ZnS

In the following a QD with a core made of ZnS and two wells made of CdSe is considered. The corresponding parameters for both semiconductors can be found in Table 2. The materials and dimensions of the QD are chosen so to allow a straightforward comparison with previous results [34], so in this case the width of the potential barrier that lies between the two potential wells and the widths of the two potential wells are kept fixed, while the core radius is used to tune the properties of the QD. In particular we choose $R_1 = R_c + 0.8$ nm; $R_2 = R_1 + 3.5$ nm, and $R_3 = R_2 + 1$ nm.

Figure 5a and b) show the lowest lying variational eigenvalues, obtained with the $\mathbf{k} \cdot \mathbf{p}$, on the conduction band and the highest ones on the valence band, as functions of the core radius. The Figure also shows the corresponding values obtained using the EMA. As it is in the case of a QDQW, both sets of values are quite similar. The proximity of the eigenvalues could lead to the conclusion that it is not necessary to go through the complications of the $\mathbf{k} \cdot \mathbf{p}$. But, as the first example analyzed in this Section shows, for small values of R_c the $\mathbf{k} \cdot \mathbf{p}$ model predicts some features that can not be found in the results obtained from the EMA approach.

Even though the spectrum shown in Figure 5 is, to some extent, quite featureless, the binding energy of the exciton that can be formed from the lowest and highest eigenvalue from the conduction and valence band,

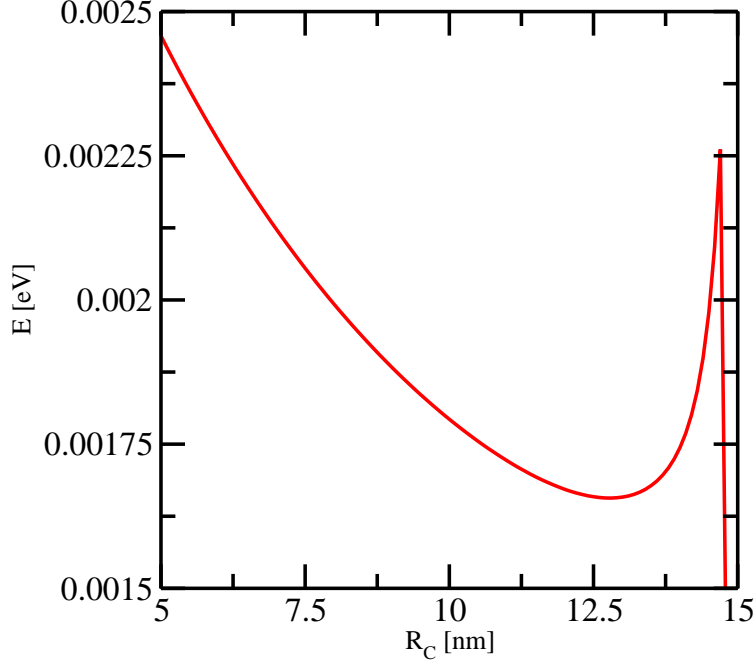


Figure 4: The binding energy calculated for an exciton trapped in a QDQW structure using the Hartree approximation together with the $\mathbf{k} \cdot \mathbf{p}$ method. The electron and hole states considered are those corresponding to the lowest and highest eigenvalue on the conduction and valence bands, respectively.

respectively, show a rather steep change around $R_c \simeq 1$ nm, see Figure 6a). The effect can be qualitatively analyzed following the radii values where the probability distributions of the electron and hole attain their maximum, this quantity is shown in Figure 6b).

The device under study is such that the outermost potential well is located between the radial coordinates $R_c + 4.3$ nm and $R_c + 5.3$ nm. So the data shown in Figure 6 shows that for $R_c \gtrsim 1$ nm the maximum of the electronic probability distribution is near the inner interface of the second potential well (*i.e.* near $R_c + 4.3$ nm), while for $R_c \lesssim 1$ nm the maximum is located nearer to the interface at $R_c + 5.3$ nm. The maximum of the hole probability distribution is always located near the outermost interface. This simple picture explains why the binding energy changes, and grows, for $R_c \lesssim 1$ nm. Of course, the change in the position of the electronic maximum must balance the effect of the polarization charges induced by the hole and electron at the interfaces, the boundary condition at the origin of the radial coordinate and the attractive force between the two particles.

4. Discussion and Conclusions

The study of spherical layered quantum dots using the $\mathbf{k} \cdot \mathbf{p}$ model remains mired by several technical difficulties: it is a coupled system of differential equations with many position-dependent parameters, and a number of matching conditions at the interfaces between the different materials. Moreover, if the exciton spectrum is to be calculated then a pair of coupled Poisson equations, which have their own set of matching conditions, must be added and solved simultaneously together with those of the $\mathbf{k} \cdot \mathbf{p}$ model. The B -spline basis set allows to calculate a variational approximation to the eigenvalues and eigenvectors, together with the electrostatic potentials and take into account all the matching and boundary conditions in an efficient way. The algebraic problem is sparse because of the “orthogonality” relationship between the B -splines, but its size grows quite fast. For instance, if the number of spline functions is N , the Hamiltonian to be diagonalized is a $8\ell N \times 8\ell N$ matrix, where ℓ is the number of angular functions used to construct

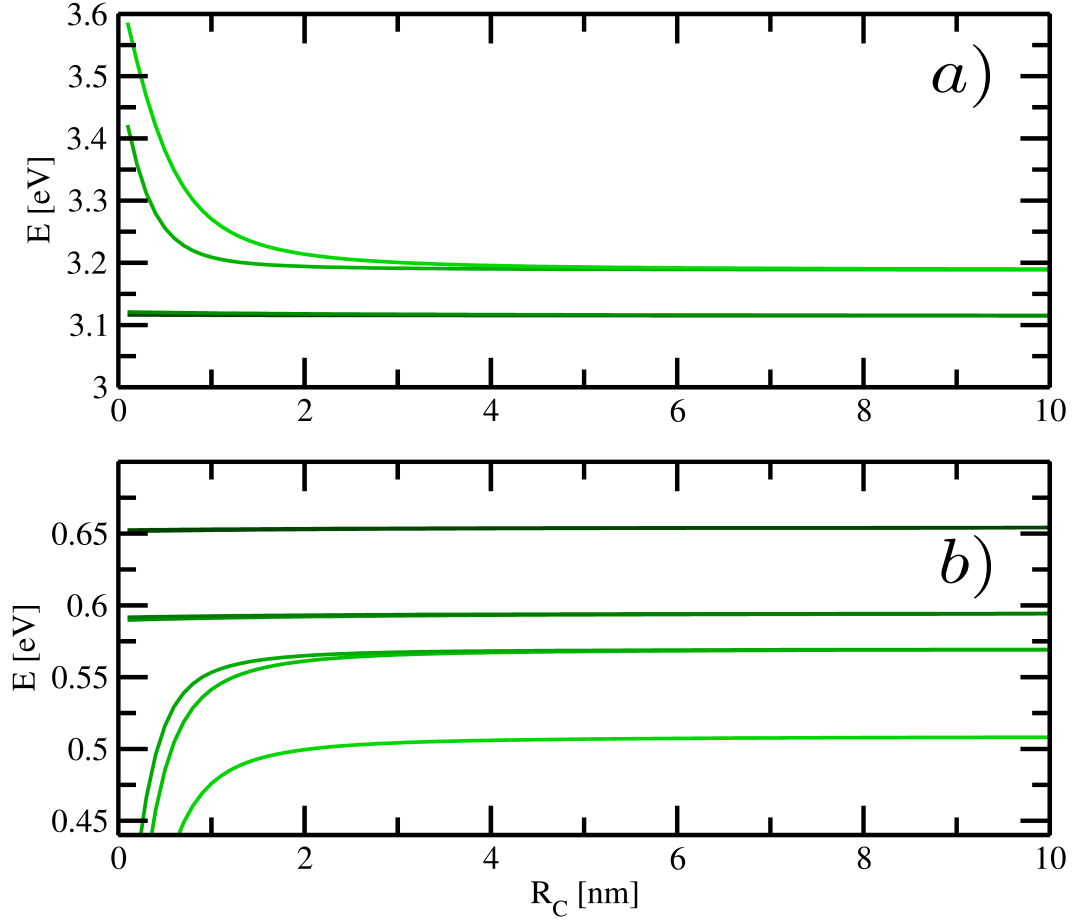


Figure 5: The variational eigenvalues calculated for the spherical structure ZnS/CdSe/ZnS/CdSe/ZnS, for both the EMA (green curves) and $\mathbf{k} \cdot \mathbf{p}$ (black curves) approaches. a) Energy levels on the conduction band. b) Energy levels on the valence band.

the variational basis, see Appendix Appendix C. In the two QD studied $N \simeq 120$, so the Hamiltonian matrices considered were, approximately, 1900×1900 matrices. The number of basis set functions used in the variational calculations is large enough to ensure that the binding energy values shown in Figure 6 have relative errors of less than 5%.

The steep change in the binding energy, observable in Figure 6, is owed to the Coulomb interaction and the polarization charges induced at the interfaces between the different materials from which the quantum dot is made. Since the change is related to changes in the localization of the electronic probability distribution it is possible that the same abrupt change can be produced applying external fields to the QD while keeping the core radius fixed. Anyway, if a external field is applied the symmetry of the problem is different and another numerical approach is required. In the same sense, to enhance the jump on the binding energy the quantum dot should be constructed with semiconductor materials with a large difference between their dielectric constants but we preferred to study combinations of materials for the potential wells and barriers that are actually constructed.

Finally, to obtain the bright and dark excitons spectrum an approach similar to the used in [30], *i.e.* using an effective electron-hole interaction that allows to control the angular momentum quantum numbers of the electron and hole wave functions, is more direct than the Hartree approach used in this paper. Nevertheless the use of the B -spline basis functions is quite flexible and allows the treatment of problems where the

Table 2: Parmetros de los materiales ZnS y $CdSe$ utilizados en el punto cuntico doble.

	E_g	E_p	Δ	ϵ	γ_1	γ_2	γ_3
ZnS	3.68 eV	20.4 eV	0.074 eV	5.7	2.12	0.51	1.56
$CdSe$	1.75 eV	17.4 eV	0.24 eV	6.3	4.4	1.6	2.68

$$\begin{aligned} \text{CBO} &= 0.9 \text{ eV} \\ \text{VBO} &= 1.03 \text{ eV} \end{aligned}$$

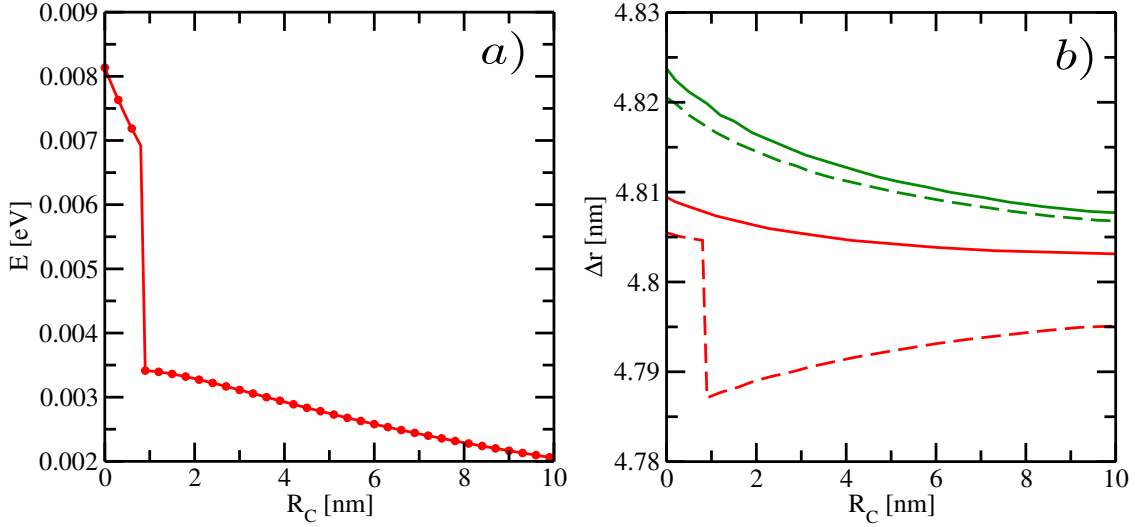


Figure 6: *a)* The binding energy calculated for an exciton trapped in a structure with a double well, using the Hartree approximation together with the $\mathbf{k} \cdot \mathbf{p}$ method. The electron and hole states considered are those corresponding to the lowest and highest eigenvalue on the conduction and valence bands, respectively. *b)* The value at which the probability distribution attains its maximum *vs* the core radius. The red dashed and continuous curves correspond to the electron probability distributions calculated for the empty QD and the Hartree approximation, respectively. The green curves correspond to the hole probability distributions and follow the same convention than the electronic ones.

exact radial wave is not available (or too convoluted) and the matching conditions of the wave functions at the material interfaces must be taken into account. We are currently working to implement an approach that computes the exciton spectrum using the effective electron-hole interaction and the B -spline variational calculation for layered quantum dots.

Acknowledgments

We acknowledge SECYT-UNC and CONICET for partial financial support of this project.

Appendix A. The B -splines functions

The B -splines functions are a generalization of the simple polynomial functions and were designed specifically as a basis to expand other functions. Thorough presentations of these functions and their properties can be found in [41] and in [42]

Let us introduce some definitions

- An order k polynomial is given by

$$p(x) = a_0 + a_1x + \dots + a_{k-1}x^{k-1},$$

i.e. it is a $k - 1$ degree polynomial.

- A sequence of points, in ascending order and not necessarily different, in the interval $[a, b]$ is called *knots*

$$\{t_i\}_{i=1, \dots, n_k}, \quad a = t_1 \leq t_2 \leq \dots \leq t_{n_k} = b.$$

A given sequence can be grouped accordingly with which elements are different as follows

$$\begin{aligned} t_1 &= t_2 = \dots = t_{\mu_1} = \zeta_1, \\ t_{\mu_1+1} &= t_2 = \dots = t_{\mu_1+\mu_2} = \zeta_2, \\ &\vdots \\ t_{n+1} &= \dots = t_{n+\mu_l+1} = \zeta_{l+1}, \quad n = \mu_1 + \dots + \mu_l. \end{aligned}$$

The points ζ_j satisfy that $\zeta_j < \zeta_{j+1}$ and split the interval $[a, b]$ in l subintervals $I_j = [\zeta_j, \zeta_{j+1}]$, and this new sequence is termed “of breakpoints”.

All in all, each B -spline is a piecewise function, defined over adjacent subintervals. In each subinterval, the B -spline is given by a polynomial of a certain order k , and satisfies a given matching condition at the point where two subintervals meet. So, a set of B -splines are determined by the order of the polynomials and the particular sequence of *knots* used in the interval $[a, b]$. The multiplicity of each *knots* prescribes the differentiability of the function in that point. A multiplicity equal to the unity results in functions that are C^{k-2} .

The more common choice for the sequence of *knots* is obtained taken *knots* $\in (a, b)$ with multiplicity equal to the unity and a *knot* in a and b with multiplicity equal to k . With this choice, the number of B -splines functions is given by

$$n_b = l + k - 1.$$

In the most general case, such that there are n_k *knots* some of them repeated, the number of B -spline functions is given by

$$n_b = n_k - k.$$

Appendix B. B -splines as a basis set to expand functions

Once the order of the polynomials, k , and the sequence of the *knots*, $\{t_i\}_{i=1, \dots, n_k} \in [a, b]$ are chosen, the set of B -splines is wholly determined. In what follows, note that we denote these functions by $B_j(x)$ or by B_j^k when there is an equation that involves B -spline functions of the same order or several different ones, since in the last case the order must be addressed explicitly. To construct the basis set it is useful to state explicitly the following properties

- In each interval (t_i, t_{i+1}) , there are only k different from zero B -splines functions

$$B_j(x) \neq 0 \quad \text{for} \quad j = i - k + 1, \dots, i. \quad (\text{B.1})$$

as a consequence

$$B_i(x) B_j(x) = 0 \quad \text{for} \quad |i - j| \geq k. \quad (\text{B.2})$$

- For all $x \in [a, b]$

$$\sum_i B_i(x) = 1. \quad (\text{B.3})$$

- The B -splines of order k can be constructed using a recurrence relationship in terms of B -spline functions of smaller orders

$$B_i^k(x) = \frac{x - t_i}{t_{i+k-1} - t_i} B_i^{k-1}(x) + \frac{t_{i+k} - x}{t_{i+k} - t_{i+1}} B_{i-1}^{k-1}(x), \quad (\text{B.4})$$

which, together with the definition of B -splines of order $k = 1$

$$B_i^1(x) = \begin{cases} 1 & \text{if } t_i \leq x \leq t_{i+1} \\ 0 & \text{otherwise} \end{cases}, \quad (\text{B.5})$$

provide the algorithm used to evaluate the B -splines at a given x value. In the book of de Boor [42] there is a number of Fortran routines that implement the algorithm implied by Equations B.4 and B.5.

Appendix C. The variational basis set used to calculate the approximate spectrum of a multilayered QD

The spectrum of a given QD is obtained by solving

$$\mathbf{H}\Psi(\mathbf{r}) = E \Psi(\mathbf{r}), \quad (\text{C.1})$$

where

$$\Psi(\mathbf{r}) = \begin{pmatrix} \psi_1(\mathbf{r}) \\ \psi_2(\mathbf{r}) \\ \psi_3(\mathbf{r}) \\ \psi_4(\mathbf{r}) \\ \psi_5(\mathbf{r}) \\ \psi_6(\mathbf{r}) \\ \psi_7(\mathbf{r}) \\ \psi_8(\mathbf{r}) \end{pmatrix}, \quad (\text{C.2})$$

where $\mathbf{H} = H(k_i \rightarrow -i\frac{\partial}{\partial x_i})$, and H is the eight band $\mathbf{k} \cdot \mathbf{p}$ Hamiltonian. Besides, we denote, for latter use, the matrix entries of the 8×8 differential operator in Equation C.1 as $H^{i,j}$ ($i, j = 1, 2, \dots, 8$).

A very accurate approximation for a number of eigenvalues can be obtained using the Rayleigh-Ritz variational model. Because the symmetry of the problem, and knowing that the atomic levels that originate the conduction and valence bands have orbital angular momentum quantum number $\ell = 0$ and $\ell = 1$, respectively, we choose a basis set with functions

$$\phi_{n,l}(\mathbf{r}) = B_n(r) P_l(\cos(\theta)), \quad (\text{C.3})$$

where the B -spline functions depend on the spherical radial coordinate, $P_l(\cos \theta)$ are the Legendre polynomials. The variational functions $\psi_i^v(\mathbf{r})$ that approximate the functions in Equation C.2 are given by

$$\psi_i^v(\mathbf{r}) = \sum_{n,l} c_{n,l}^i \phi_{n,l}(\mathbf{r}), \quad i = 1, \dots, 8. \quad (\text{C.4})$$

The variational spectrum is calculated solving the *matricial* eigenvalue problem

$$[\mathbf{H}]\mathbf{c} = E^v \mathbf{S}\mathbf{c}, \quad (\text{C.5})$$

where the vector \mathbf{c} has components $c_{n,l}^i$, the matrix elements of $[\mathbf{H}]$ are given by

$$[\mathbf{H}]_{n,l,n',l'}^{i,j} = \langle B_n P_l | \mathbf{H}^{i,j} | B_{n'} P_{l'} \rangle, \quad (\text{C.6})$$

and the matrix elements of the overlapping matrix \mathbf{S} can be written as

$$[\mathbf{S}]_{n,l,n',l'}^{i,j} = \langle B_n P_l | B_{n'} P_{l'} \rangle \delta_{i,j}, \quad (\text{C.7})$$

where δ is the usual Kronecker delta.

If the basis set size is N , then the Hamiltonian matrix in Equation C.5 is a $8N \times 8N$ matrix, because of this and since the number of B -splines functions is related to the number of *knots* the Hamiltonian matrix may become very large. Anyway, the relationship in Equation B.2 imposes that the Hamiltonian matrices would be sparse matrices indeed.

To evaluate the matrix elements in Equation C.6 it is necessary to write down all the Cartesian derivatives in the differential operator \mathbf{H} as derivatives on the spherical coordinates, then all the integrals in radial coordinates can be obtained using a highly efficient Gauss-Legendre quadrature method. The integrals that depend on the polar angle can be calculated analytically.

In all the numerical evaluations, the radial coordinate was considered bounded for a value R_{max} large enough, in particular quite larger than the characteristic radii of the QD (core, internal and external well radius, etc).

For a layered QD with a single well, the integration interval for the radial coordinate $[0, R_{max}]$ was split in three subintervals, each one corresponds to the core, well and barrier parts of the QD, *i.e.* $[0, R_c]$, $[R_c, R_1]$ y $[R_1, R_{max}]$. In each interval the distribution of the *knots* was chosen uniform, with 45 *knots* for the first and second subintervals, while for the last one the number of *knots* was taken equal to 30. Besides $R_{max} = 50 \text{ nm}$.

For a layered QD with two wells, the interval $[0, R_{max}]$ was split in five subintervals $[0, R_c]$, $[R_c, R_1]$, $[R_1, R_2]$, $[R_2, R_3]$ y $[R_3, R_{max}]$. The distribution of *knots* in each subinterval was chosen uniform, with 25 *knots* for the first, second, third and fourth subintervals, while for the last subinterval 20 *knots* were used. In this case $R_{max} = 30 \text{ nm}$.

References

- [1] A. R. Kortan, R. Hull, R. L. Opila, M. G. Bawendi, M. L. Steigerwald, P. J. Carroll, and L. E. Brus, *J. Am. Chem. Soc.* **112**, 1327, (1990).
- [2] H. S. Zhou, I. Honma, H. Komiyama, and J. W. Haus *J. Phys. Chem.* **97**, 895 (1993).
- [3] A. Mews, A. Eychemueller, M. Giersig, D. Schooss, and H. Weller, *J. Phys. Chem.* **98**, 934 (1994).
- [4] L. P. Kouwenhoven, D. G. Austing, and S. Tarucha, *Rep. Prog. Phys.* **64**, 701, (2001).
- [5] J. W. Haus, H. S. Zhou, I. Honma, and H. Komiyama, *Phys. Rev. B* **47**, 1359 (1993).
- [6] D. Schooss, A. Mews, A. Eychemüller, and H. Weller, *Phys. Rev. B* **49**, 17072 (1994).
- [7] G. W. Bryant, *Phys. Rev. B* **52**, R16997 (1995).
- [8] L. Bánya, P. Gilliot, Y. Z. Hu, and S. W. Koch, *Phys. Rev. B* **45**, 14136 (1992).
- [9] K. Chang K and J. Xia, *Phys. Rev. B* **57**, 9780 (1998).
- [10] A. Muller, Q. Q. Wang, P. Bianucci, C. K. Shih, and Q. K. Xue, *Appl. Phys. Lett.* **84** (2004), 981 (2004).
- [11] Byoung-Ho Kang, Jae-Sung Lee, Sang-Won Lee, Sae-Wan Kim, Jun-Woo Lee, Sai-AnandGopalan, Ji-Sub Park, Dae-Hyuk Kwon, Jin-Hyuk Bae, Hak-Rin Kim, and Shin-Won Kang, *Sci. Rep.-UK* **6**, 34659 (2016)
- [12] H. Shen, S. Wang, H. Wang, J. Niu, L. Qian, Y. Yang, A. Titov, J. Hyvonen, Y. Zheng, and L. S. Li, *ACS Appl. Mater. Interfaces* **5**, 4260 (2013).
- [13] A. D. Yoffe, *Adv. Phys.* **42**, 173 (1993)
- [14] U. Woggon and S. V. Gaponenko, *Phys. Stat. Sol. (b)* **189**, 285 (1995).
- [15] L. Wang Wang and A. Zunger, *J. Phys. Chem.* **98** 2158, (1994).
- [16] A. Franceschetti and A. Zunger, *Phys. Rev. Lett.* **78**, 915 (1997).
- [17] S. Ögüt, J. R. Chelikowsky, and S. G. Louie, *Phys. Rev. Lett.* **79**, 1770 (1997).
- [18] B. Billaud, M. Picco, and T. T. Truong, *J. Phys.: Condens. Matter* **21**, 395302 (2009).
- [19] W. Yao *et al.*, *J. Nanosci. Nanotechno.* **10**, 7612 (2010).
- [20] G. Bastard, *Wave mechanics applied to semiconductor heterostructures* (Les Editions de Physique: Paris, 1990)
- [21] L. C. Lew Yan Voon and M. Willatzen, *The kp method* (Springer-Verlag: Berlin Heidelberg, 2009)
- [22] D. Stier, M. Grundmann, and D. Bimberg, *Phys. Rev. B* **59**, 5688 (1999).
- [23] M. Winkelnkemper, A. Schliwa, and D. Bimberg, *Phys. Rev. B* **74**, 155322 (2006).

- [24] H. Jiang y J. Singh, *Phys. Rev. B* **56**, 4696 (1997).
- [25] W. Jaskolski and G. W. Bryant, *Phys. Rev. B* **57**, R4237 (1998)
- [26] C. Pryor, *Phys. Rev. B* **57**, 7190 (1998).
- [27] Jingbo Li y Jian-Bai Xia, *Phys. Rev. B* **61**, 15880 (2000).
- [28] Y. Kayanuma, *Phys. Rev. B* **38**, 9797 (1988).
- [29] T. Takagahara, *Phys. Rev. B* **47**, 4569 (1993).
- [30] A. V. Rodina and A. L. Efros, *Phys. Rev. B*, **93**, 155427 (2016).
- [31] A. Zrenner, E. Beham, S. Stuffer, F. Findeis, M. Bichler, and G. Abstreiter, *Nature* **418**, 612 (2002).
- [32] H. J. Krenner, S. Stuffer, M. Sabathil, E. C. Clark, P. Ester, M. Bichler, G. Abstreiter, J. J. Finley, and A. Zrenner, *New J. Phys.* **7**, 184 (2005).
- [33] A. Ferrón, P. Serra, and O. Osenda, *Phys. Rev. B* **85**, 165322 (2012).
- [34] A. Ferrón, P. Serra, and O. Osenda, *J. Appl. Phys.* **113**, 134304 (2013).
- [35] V. Holovatsky, I. Bernik, M. Yakhnevych, *Physica B* **508**, 112 (2017).
- [36] V. Holovatsky, I. Bernik, M. Yakhnevych, *Physica E* **83**, 256 (2016).
- [37] F. Karaca Boz, B. Nisanci, S. Aktas, S. Erol Okan, *Appl. Surf. Sci.* **387**, 76 (2016).
- [38] F. H. Alharbi *et al.*, *J. Phys.: Conf. Ser.* **707**, 012010 (2016)
- [39] V. V. Ravi Kishore, N. Čukarić, B. Partoens, M. Tadić, and F. M. Peeters, *J. Phys.: Condens. Matter* **24**, 135302 (2012).
- [40] V. V. Ravi Kishore, B. Partoens and F. M. Peeters, *J. Phys.: Condens. Matter* **26**, 095501 (2014).
- [41] H. Bachau, E. Cormier, P. Decleva, J. E. Hansen, and F. Martín, *Rep. Prog. Phys.* **64**, 1815 (2001).
- [42] C. de Boor *A practical guide to splines* (New York: Springer, 1978)
- [43] M. Garagiola, F. M. Pont, and O. Osenda, *J. Phys. B: At. Mol. Opt. Phys.* **51**, 075504 (2018).
- [44] J. M. Ferreyra and C. R. Proetto, *Phys. Rev. B* **60**, 10672 (1999).
- [45] J. M. Ferreyra and C. R. Proetto, *Phys. Rev. B* **57**, 9061 (1998).